Editors' Suggestion

Electrothermal Manipulation of Current-Induced Phase Transitions in Ferrimagnetic $Mn_3Si_2Te_6$

Jiaqi Fang,[1,2,*] Jiawei Hu,[1,2,*] Xintian Chen,[1,2,*] Yaotian Liu,[1,2] Zheng Yin,[1,2] Zhe Ying,[1] Yunhao Wang,[1,2] Ziqiang Wang,[3] Zhilin Li,[1,2,†] Shiyu Zhu,[1,2,‡] Yang Xu,[1,2,§] Sokrates T. Pantelides,[4,2] and Hong-Jun Gao[1,2,5,‖]

[1]*Beijing National Laboratory for Condensed Matter Physics, Institute of Physics, Chinese Academy of Sciences, Beijing 100190, China*
[2]*School of Physical Sciences, University of Chinese Academy of Sciences, Beijing 100049, China*
[3]*Department of Physics, Boston College, Chestnut Hill, Massachusetts 02467, USA*
[4]*Department of Physics and Astronomy and Department of Electrical and Computer Engineering, Vanderbilt University, Nashville, Tennessee 37235, USA*
[5]*Hefei National Laboratory, 230088 Hefei, Anhui, China*

(Received 5 February 2025; accepted 22 May 2025; published 25 June 2025)

Phase transitions driven by external parameters are fundamental to condensed matter physics, providing critical insights into symmetry breaking and emergent phenomena. Recently, ferrimagnetic $Mn_3Si_2Te_6$ has attracted considerable attention for its magnetic-field-induced insulator-metal transitions and current-driven phase transitions, but the role of applied currents in the magnetic phase remains poorly understood. Here, we employ local magnetization probes and time-resolved transport measurements to investigate the current-induced phase transitions. Magnetic force microscopy with controlled current flow reveals the evolution of ferrimagnetic domains and a first-order-like magnetic phase transition with an abrupt voltage jump. The measurements with rectangular pulsed currents reveal that the time evolution of resistance closely mirrors the resistance-temperature profile, highlighting the role of heat accumulation and a positive-feedback mechanism in the current-induced phase transitions. Furthermore, we demonstrate that the intrinsic current-voltage characteristics adhere to Ohm's law, displaying linearity across various magnetic fields and temperatures. Our work advocates for a cautious approach in distinguishing between genuine current-induced nonequilibrium quantum states and thermal effects.

DOI: 10.1103/ry2d-bgyy

Electric currents or fields can introduce emergent nonequilibrium quantum states and phase transitions, such as the electromagnetic radiation-induced superconductivity [1] and electrically driven insulator-metal transitions (IMTs) in strongly correlated systems (e.g., in VO_2, Ca_2RuO_4, Sr_2IrO_4) [2,3]. These IMTs are often accompanied by sharp resistance change, negative differential resistance (NDR), bistable switching, magnetic transitions or structural modifications, making them suitable candidates for logic and memory electronics [2–7]. Several reports have suggested that current-induced IMTs arise through potential mechanisms such as Mott gap suppression [8,9], field-induced effective carrier concentration [10], electroforming [11,12], spin-orbit interaction, magnetoelastic coupling [3], or conventional electrical breakdown. However, in many cases, unambiguous evidence for the genuine nonequilibrium steady states after the transitions remains elusive, largely due to limitations in detection methods and the intricate interplay of different mechanisms, including unavoidable Joule heating that drives the system into higher-temperature phases [2,13–15]. Additionally, some systems simultaneously exhibit electronic, magnetic, and structural phase modifications, further complicating the analysis [9,16] (e.g., spurious diamagnetic signals induced by Joule heating of the sample and holder [17]). Various efforts have been devoted to identify thermal effects, such as placing thermometers closer to the sample [18,19], thermal imaging [20,21], Raman spectroscopy [22], and tracking anisotropic evolution of lattice constants [3]. Despite numerous efforts, experimentally distinguishing and precisely controlling electrothermal effects from nonthermal origins remains fundamentally challenging.

$Mn_3Si_2Te_6$ has recently emerged as a novel layered ferrimagnet with alternating stacking of honeycomb and triangular lattices of Mn atoms, whose spins are predominantly lying within the *ab* plane [Fig. 1(a)] [23–26]. An out-of-plane magnetic field can drive IMTs, manifesting as colossal magnetoresistance with strong anisotropic field dependences [23–29]. The spin orientation and its coupling to the orbital degree of freedom have been proposed to control the splitting of topological nodal lines and give rise to an efficient gap closing near the Fermi

*These authors contributed equally to this work.
†Contact author: lizhilin@iphy.ac.cn
‡Contact author: syzhu@iphy.ac.cn
§Contact author: yang.xu@iphy.ac.cn
‖Contact author: hjgao@iphy.ac.cn

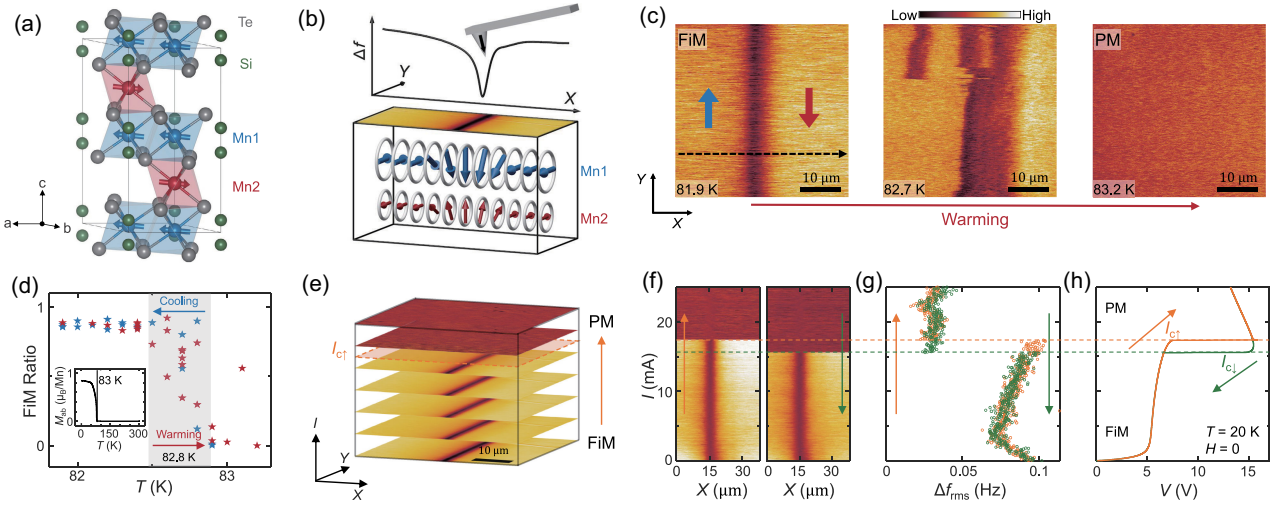

FIG. 1. (a) Crystal and magnetic structure of $Mn_3Si_2Te_6$ below T_c. (b) Average MFM line profile (top), MFM mapping (43×43 μm^2 at $T = 25$ K) and schematic of spin structure across the FiM domain wall (bottom). The color scale is 1.2 Hz. (c) Temperature-dependent MFM mapping. As sample warmed from 81.9 K (below T_c) to 83.2 K (above T_c), the FiM domain wall expands and evolves to a PM phase. (d) The FiM region ratio extracted from MFM images measured at different temperatures across T_c. Inset: temperature dependence of the ab-plane magnetization M_{ab} at $\mu_0 H = 10$ mT, showing FiM-PM transition at $T_c = 83$ K. (e) Stack of MFM images from $I = 0$ to 17.5 mA at $T = 20$ K. As current increases, the FiM phase transits to the PM phase at $I_{c\uparrow}$. The color scales vary slightly for clarity. (f)–(h) Repeated MFM line scans [along the black dashed arrow in (c)] (f), the corresponding root-mean-square value Δf_{rms} (g), and the measured voltage V while the current I is varied (y axis) at 20 K (h), showing consistent sharp transitions at critical currents $I_{c\uparrow} = 17.4$ mA (sweeping up) and $I_{c\downarrow} = 15.6$ mA (sweeping down). The voltage V and MFM signals are recorded simultaneously.

level [26,28,30,31]. In another work, Zhang *et al.* reported the observation of peculiar current-induced transport behaviors, i.e., first-order-like phase transition and time-dependent bistable switching, as hallmarks of the existence of chiral orbital currents (COCs) that can couple to the ferrimagnetic (FiM) state and flow spontaneously along edges of $MnTe_6$ octahedra in $Mn_3Si_2Te_6$ [4].

Here we report a study combining current-modulated local magnetization microscopy and time-resolved transport measurements on bulk samples of $Mn_3Si_2Te_6$ to scrutinize the effect of current flow. In the magnetic force microscopy (MFM) measurements, we observe a hysteretic magnetic phase transition via evolution of magnetic domains under direct currents. Further pulsed currents reveal that the detailed time evolution of the resistance closely mirrors the resistance-temperature (R-T) profile. We highlight that under tens of milliamperes the real sample temperature (T_s) can be raised by > 100 K in less than 1 ms. Such self-heating drives the sample into a higher-temperature nonmagnetic and semiconducting phase, consistently explaining our observations. We further demonstrate the intrinsic current-voltage relation of $Mn_3Si_2Te_6$ to have linear characteristics.

To investigate the microscopic magnetic characteristics, we first conduct temperature-dependent MFM measurements on a $Mn_3Si_2Te_6$ sample. At $T = 25$ K (far below Curie temperature T_c) and zero magnetic field ($H = 0$), the in-plane FiM domains manifest as bright regions in the mapping of Δf (resonance frequency shift of the tip), separated by a transverse dark domain wall [Fig. 1(b)]. These FiM domains shrink and expand easily under small in-plane magnetic fields in the Y direction, suggesting their magnetization in parallel or antiparallel with the domain wall (see Supplemental Material Fig. S1 [32]).

The evolution of magnetic domains with increasing temperature is shown in Fig. 1(c). As the sample warms up through T_c, the width of the domain wall expands and the sample evolves from FiM to the paramagnetic (PM) phase at $T > T_c$ (more details are shown in Supplemental Material Fig. S2 [32]). A quantitative evolution of the magnetic state is revealed by the extracted FiM ratio obtained from analyzing the Δf distribution of the FiM domain wall [Fig. 1(d)]. A dramatic change of the FiM region ratio around $T_c \sim 82.8$ K is observed, indicating a temperature-driven magnetic phase transition. This observation is consistent with the global magnetization measurements performed along the ab plane [inset of Fig. 1(d)].

We next study the current-driven phase transition [4] by supplying direct-current flow through the sample. The MFM mapping reveals an FiM state at low currents, indicated by domain and domain wall signals, and a nonmagnetic state at high currents, with no detectable MFM contrast [Fig. 1(e)]. To perform continuous MFM measurements, the tip is maintained at a constant height above the sample and scanned across the domain wall, while the direct current is swept upward or downward. During the current ramping-up process, the domain wall signal first persists and barely changes, suggesting a robust

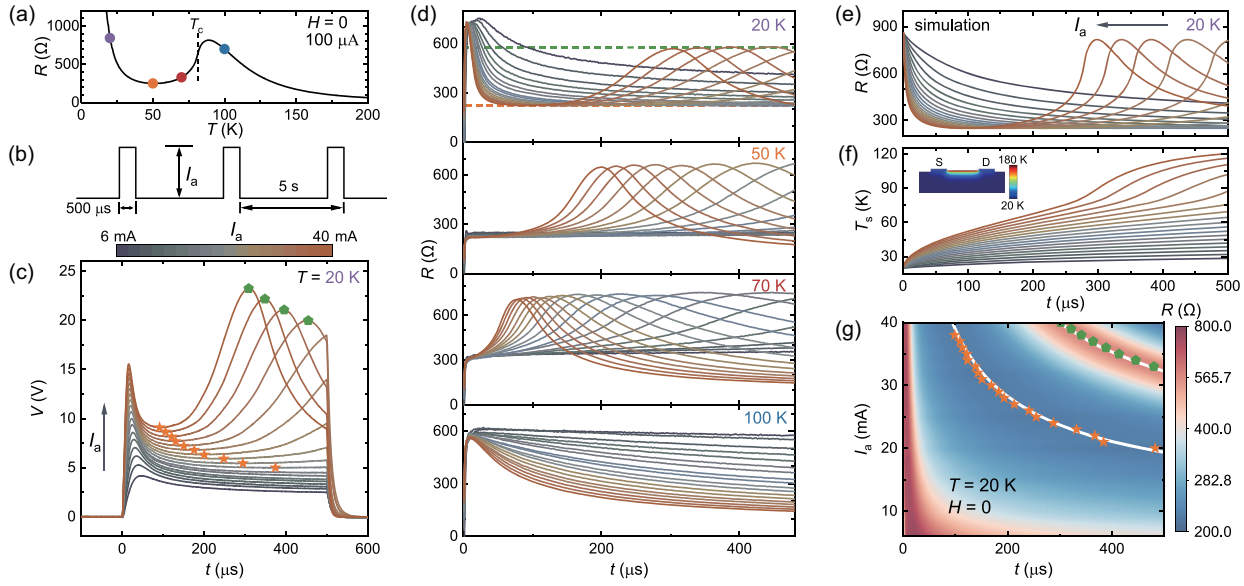

FIG. 2. (a) Resistance as a function of the temperature measured with a small dc $I = 100$ μA. (b) Schematic diagram of the repetitive current pulses with duration ∼500 μs and periodicity ∼5 s. (c) Voltage response at various pulse amplitudes (I_a) as a function of time t at 20 K. The curves are color coded according to the legend bar and take intervals of 2 mA. The arrow indicates the direction of increasing I_a. (d) Resistance $R(= V/I)$ as a function of time ($0 \sim 480$ μs) with increasing I_a (gray to orange curves) at 20, 50, 70, and 100 K, corresponding to the purple, orange, red, and blue dots in (a), respectively. (e),(f) Time-dependent resistance and sample temperature (T_s) with varying pulse amplitudes at 20 K, simulated from a simplified Joule-heating model described in the main text. The inset graph is the cross-sectional diagram showing the temperature gradient across the sample (placed on a thick Si substrate) after applying a 40 mA current for a duration of ∼500 μs, simulated by COMSOL. S and D stand for source and drain, respectively. (g) Color mapping of the resistance as a function of t and I_a [same data as the top panel of (d)], with the corresponding dips and peaks in $R(t)$ marked by the orange stars and green pentagons, respectively. The dip and peak positions extracted from the simulation are illustrated as white lines.

FiM state. However, when the current surpasses a threshold or critical value of $I_{c\uparrow} \sim 17.4$ mA, we observe a significant change in MFM signals and a sudden disappearance of the domain wall [Fig. 1(f), left]. The magnetic features observed beyond the critical currents are similar to those of the PM phase above T_c in Fig. 1(c). This behavior indicates that a nonmagnetic phase emerges at larger currents. Similarly, during the current-reduction process, the FiM state is recovered below a smaller critical value of $I_{c\downarrow} \sim 15.6$ mA, showing hysteretic behavior [Fig. 1(f), right]. The quantitative evolution of the current-dependent magnetic state is further revealed by the root mean square of the MFM line scan (Δf_{rms}) [Fig. 1(g)].

The four-terminal I-V curves, measured simultaneously with the MFM mappings, exhibit strong nonlinearity and hysteretic transitions at the critical currents $I_{c\uparrow}$ and $I_{c\downarrow}$ [Fig. 1(h)]. The slope of the I-V relationship is small under low currents, followed by a relatively broad region where the voltage changes gradually before reaching the critical current. The abrupt change of the voltage signals at the transition and the resulting NDR ($dV/dI < 0$) at $I > I_c$ are reminiscent of the first-order and bistable switching previously observed for $Mn_3Si_2Te_6$ [4], as well as the electric-field-driven IMTs observed in many transition-metal compounds [2]. It is hence crucial to investigate the origins of the current-induced switching and the NDR associated with the nonmagnetic phase $I > I_c$. Given that the resistance well exceeds a kilohm (kΩ) at low temperatures, a current above a milliamp (mA) could induce substantial Joule heating that cannot be safely neglected [2,39]. Therefore, electrothermal effects need to be carefully examined.

In typical transport measurements, dc or small-frequency ac with time resolution ∼100 ms for the data acquisition were employed to obtain the electrical responses, where any transient information associated with the fast current-driven transitions cannot be well resolved. In Fig. 2(a), we first show the R-T curve measured at small excitation currents (100 μA used here) for a different $Mn_3Si_2Te_6$ sample, consistent with previous measurements [24,27,28]. The sample exhibits thermal-activated semiconducting behavior ($dR/dT < 0$) at both higher temperatures ($> \sim 90$ K) and lower temperatures ($< \sim 50$ K), with a metallicliike behavior ($dR/dT > 0$) at intermediate temperatures. We then employ a four-channel oscilloscope to achieve microseconds (μs) temporal resolution, enabling precise control and detection of the first-order-like switching [14,40–43]. The transient four-terminal voltage V and current through the sample I are recorded simultaneously in real time. To characterize the sample's response, we apply both triangular waveform (see Supplemental Material Fig. S4 [32]) and rectangular waveform [Fig. 2(b)]. The rectangular current pulse has an onset duration of 500 μs

and an amplitude of I_a, followed by a delay time of ~5 s (repetition rate $f = 0.2$ Hz) to avoid any accumulative heating.

We now focus on the electrical responses within the 500 μs current pulse. The measurements are performed with varying I_a at cryostat temperatures T of 20, 50, 70, and 100 K [color coded and highlighted by the circles in the R-T curve shown in Fig. 2(a)], with an example of the real-time voltage response at $T = 20$ K shown in Fig. 2(c). As demonstrated at $T = 20$ K, the response strongly depends on the current pulse amplitude, varying from 6 to 40 mA. At small I_a, it features a sharp initial rise and a long decay afterward. With increasing I_a, the decay in V slowly evolves into an upturn (showing a broad dip) and then a peak feature emerges at large currents. The larger I_a results in faster onsets of the minima (marked by the star symbols) and maxima (marked by the pentagon symbols) in Fig. 2(c). Combining the measured real-time current $I(t)$, we can obtain the time dependences of the resistance with $R(t) = V(t)/I(t)$ in Fig. 2(d) [32] (also shown here for the results at $T = 50$, 70, and 100 K). Interestingly, as illustrated by the orange (green) horizontal dashed lines in the top panel of Fig. 2(d), the minima (maxima) collapse to the same resistance value, ~220 Ω (~600 Ω) after the scaling. The initial rise of the resistance curves within a few microseconds is attributed to the charging of the parasitic capacitance (estimated to be ~300 pF) in the cryogenic circuits. Similarly, there is a discharging effect at the end of each current pulse [Fig. 2(c)].

While the evolution of the resistance with respect to time at 50 and 70 K does not show the dip feature, the resistance maxima still exist, exhibiting a trend of shorter onset time with increases in I_a and T. The values of the resistance maxima increase slightly compared to those at 20 K. As the temperature rises to 100 K, the time-dependent resistance only exhibits a long-decaying feature that goes to lower values at larger I_a. We also notice that the real-time resistance evolution measured at the four different cryostat temperatures (20, 50, 70, or 100 K) with large currents (e.g., the orange curves) in Fig. 2(d) closely resembles the segments of the R-T curve at higher temperatures (than that marked by the colored dot symbols) in Fig. 2(a), indicating a strong correlation between time progression and temperature increase in the pulsed-current measurements.

In the following analysis, we will show that the cumulative Joule heating produced by the current can well explain the experimental observations. We employ a simplified electrothermal model simulation for further examination. The temporal evolution of the sample temperature T_s (assumed uniform for simplicity) is governed by the balance between Joule heating and thermal dissipation, described by $C(\mathrm{d}T_s/\mathrm{d}t) = I^2R - K(T_s - T_0)$, where C is the sample heat capacity, K is the interfacial thermal conductance (see more details in Supplemental Material [32]), and T_0 is the cryostat temperature (read by the thermometer). During the short-time measurements, T_0 is held constant. The parameters C, K, and R are temperature dependent. To approximate the complexity of heat exchange between the sample and its environment, K is modeled using a second-order polynomial fit [44]. The resistance R is calculated via Ohm's law ($R = V/I$), assuming no current dependence [data extracted from Fig. 2(a)]. Using this framework, we simulate the time evolution of R for varying pulse amplitudes I_a [e.g., simulated results at $T = 20$ K in Fig. 2(e)] and the corresponding increase in T_s [Fig. 2(f)]. The simulated R-t curves reproduce the key features observed experimentally [top panel of Fig. 2(d)]. Upon current application ($t = 0$), Joule heating drives T_s upward, and R evolves according to the temperature-dependent R-T curve. Higher currents induce faster heating and larger temperature increases. The simulated onset times for resistance peaks and dips [white curves in Fig. 2(g)] align with experimental data (symbols), as visualized in the resistance color map.

The simulation indicates that the sample temperature can rise rapidly by more than ~100 K within the short current pulse (far off from the cryostat temperature T read by the thermometer). We note that the resistance peaks in Fig. 2(d) are slightly broader and have smaller values than the maximal resistance ~860 Ω in Fig. 2(a). This should be due to the inhomogeneous heating in the bulk sample, as can be seen from the temperature distribution simulated using COMSOL in the inset of Fig. 2(f).

To rule out the impact by Joule heating on the I-V curves, we further validate our analyses by extracting the intrinsic I-V characteristics from the pulsed-current measurements [Figs. 3(a) and 3(b)]. The sample voltage V and current I are recorded shortly after the onset of the current pulse (delay time $t = 7.5$ μs used here) when no substantial Joule heating is involved. We note that such methods have been extensively used for obtaining the intrinsic I-V characteristics under large electric fields or currents [39,42,43]. Here, the obtained I-V curves for $Mn_3Si_2Te_6$ exhibit linear relationships at all the measured magnetic fields and temperatures; i.e., they obey Ohm's law. This result is in direct contrast to the slow dc measurements that show critical-current-like behaviors [see Supplemental Material Fig. S3(b) [32]].

In the upper panel of Fig. 3(c), we directly compare the I-V curves obtained from pulsed (purple) with dc (black) measurements at a representative temperature of 20 K. The two curves overlap closely in the low-current regime ($I < \sim 1$ mA) but diverge significantly at higher currents. Notably, the sharp transition and NDR observed in the dc curve are absent in the intrinsic I-V curve. Furthermore, the resistance $R(= V/I)$ calculated from the dc I-V curve [lower panel of Fig. 3(c)] exhibits a nonmonotonic dependence on current, mirroring its temperature-dependent evolution over the range $\sim 20 < T < \sim 140$ K [Fig. 3(d)]. Regions of correspondence between the current- and

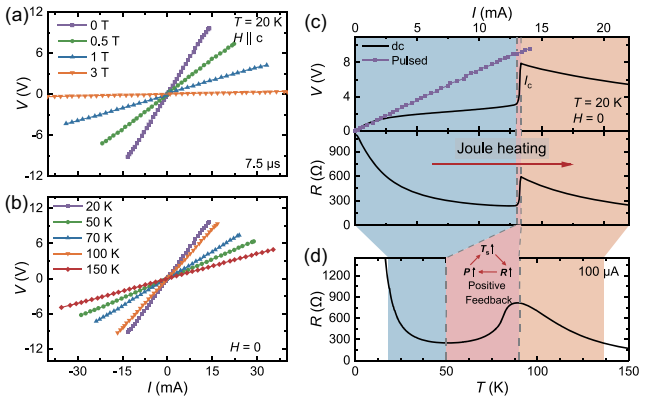

FIG. 3. (a),(b) I-V characteristic extracted from pulsed-current measurement (delay time 7.5 μs) at various magnetic fields ($T = 20$ K) (a) and at various temperatures ($H = 0$) (b). (c) Upper panel: comparison of I-V curves from the dc measurement (in black) and pulsed-current measurement (in purple) at 20 K and $H = 0$. Lower panel: resistance (calculated by V/I from the dc measurement) as a function of the current. (d) Replotted R-T curve [same data as Fig. 2(a)], strongly resembling the R-I curve. The color blocks serve as guides for corresponding segments in each curve. Inset:diagram of a positive-feedback process for the transition region (highlighted by the pink blocks), where the sample temperature (T_s), resistance (R), and power ($P = I^2R$) have a positive correlation with increasing the current (I). This process promotes a steeper rise in the V-I or R-I curve compared to the R-T curve within the pink region.

temperature-dependent resistance are color coded (blue, pink, orange). A key distinction arises in the pink regions, where the resistance increase at the critical current $I_c \sim 13$ mA is markedly sharper than the analogous temperature-driven rise in the range $50 < T < 90$ K. This discrepancy is attributed to Joule heating and an associated positive-feedback mechanism. During dc measurements, initial current increases gradually heat the sample to ~50 K, resulting in a negative R-I dependence (blue region) due to the intrinsic decrease of resistance with temperature ($dR/dT < 0$). Beyond this point, further current increases raise the sample temperature (T_s), driving R upward. This enhances the Joule power ($P = IV = I^2R$), which further promotes a rise in T_s through the positive-feedback loop [Fig. 3(d), inset]. Consequently, the R-I curve in the pink region exhibits a steeper rise at I_c compared to the R-T behavior, reflecting the self-reinforcing interplay between heating and resistance.

The temperature rise is accelerated through the positive-feedback region ($dR/dT > 0$, pink region), resulting in sharp "current-driven" or "first-order-like" transition behavior in the dc V-I or V-t measurements. Under magnetic fields, the resistance exhibits a more pronounced temperature dependence in this regime, leading to a sharper transition [see Supplemental Material Fig. S3(b) [32]]. Above I_c, the sample temperature exceeds T_c, entering a regime where resistance decreases with temperature ($dR/dT < 0$, orange region). This produces the observed NDR in the I-V curves and correlates with the absence of magnetic domains in MFM measurements. We emphasize that analogous Joule-heating mechanisms have been implicated in current- or field-driven NDR phenomena in classic transition-metal oxides, such as vanadium, titanium, and niobium oxides [2]. These parallels underscore the universality of electrothermal feedback in driving abrupt electronic transitions.

Thermal effects typically require longer timescales to reach equilibrium and often induce time delays and hysteretic behaviors in transport measurements. For instance, the time-dependent bistable switching (Zhang *et al.* [4] and Supplemental Material Fig. S5 [32]) with long timescales (seconds to minutes) operates only for currents slightly exceeding I_c. This delay arises because the sample requires time to accumulate sufficient energy via Joule heating to enter the positive-feedback regime ($T > \sim 50$ K), where abrupt bistable switching occurs.

In summary, systematic MFM and dynamical transport measurements in $Mn_3Si_2Te_6$ reveal that Joule heating at high currents plays a critical role in driving the observed current-induced phase transitions. The first-order-like phase transition triggered by direct currents arises from self-reinforcing heat accumulation via a positive feedback mechanism, enabling the sample temperature to surge by over ~100 K within hundreds of microseconds. Our findings underscore the critical need to account for electrothermal dynamics when interpreting transport phenomena in quantum materials. While no definitive evidence of COC domains [4] is observed in this study, their potential existence cannot be excluded and necessitates future investigations using advanced techniques with higher magnetic sensitivity and spatial resolution.

Note added—Recently, we became aware of two independent works discussing the pivotal role of Joule heating in $Mn_3Si_2Te_6$ under large currents [45,46].

Acknowledgments—This work was funded by National Natural Science Foundation of China (Grants No. 12174439, No. 62488201, No. 12374199), the Innovation Program for Quantum Science and Technology (Grants No. 2021ZD0302400 and No. 2021ZD0302300). Crystal growth by Z. L. was supported by the Youth Innovation Promotion Association of CAS (No. 2021008).

Data availability—The data that support the findings of this Letter are openly available [47].

[1] A. Cavalleri, Contemp. Phys. **59**, 31 (2018).
[2] A. L. Pergament, G. B. Stefanovich, and S. D. Khanin, Electronic switching and metal-insulator transitions in compounds of transition metals, in *Condensed Matter at*

the Leading Edge, edited by M. P. Das (Nova Science Publishers, Hauppauge, NY, 2006), Chap. 1, pp. 1–67.
[3] G. Cao, J. Phys. Condens. Matter **32**, 423001 (2020).
[4] Y. Zhang, Y. Ni, H. Zhao, S. Hakani, F. Ye, L. DeLong, I. Kimchi, and G. Cao, Nature (London) **611**, 467 (2022).
[5] R. Waser and M. Aono, Nat. Mater. **6**, 833 (2007).
[6] You Zhou and S. Ramanathan, Proc. IEEE **103**, 1289 (2015).
[7] Z. Yang, C. Ko, and S. Ramanathan, Annu. Rev. Mater. Res. **41**, 337 (2011).
[8] R. Okazaki, Y. Nishina, Y. Yasui, F. Nakamura, T. Suzuki, and I. Terasaki, J. Phys. Soc. Jpn. **82**, 103702 (2013).
[9] C. T. Suen *et al.*, Nat. Phys. **20**, 1757 (2024).
[10] G. Stefanovich, A. Pergament, and D. Stefanovich, J. Phys. Condens. Matter **12**, 8837 (2000).
[11] F. Chudnovskii, L. Odynets, A. Pergament, and G. Stefanovich, J. Solid State Chem. **122**, 95 (1996).
[12] J. Joshua Yang, F. Miao, M. D. Pickett, D. A. A. Ohlberg, D. R. Stewart, C. N. Lau, and R. S. Williams, Nanotechnology **20**, 215201 (2009).
[13] G. Mattoni, S. Yonezawa, F. Nakamura, and Y. Maeno, Phys. Rev. Mater. **4**, 114414 (2020).
[14] F. A. Chudnovskii, A. L. Pergament, G. B. Stefanovich, P. Somasundaram, and J. M. Honig, Phys. Status Solidi (a) **162**, 601 (1997).
[15] J. Duchene, J. Solid State Chem. **12**, 303 (1975).
[16] G. Cao, J. Terzic, H. D. Zhao, H. Zheng, L. E. De Long, and P. S Riseborough, Phys. Rev. Lett. **120**, 017201 (2018).
[17] G. Mattoni, S. Yonezawa, and Y. Maeno, Appl. Phys. Lett. **116**, 172405 (2020).
[18] G. Avallone, R. Fermin, K. Lahabi, V. Granata, R. Fittipaldi, C. Cirillo, C. Attanasio, A. Vecchione, and J. Aarts, npj Quantum Mater. **6**, 91 (2021).
[19] G. Mattoni, K. Fukushima, S. Yonezawa, F. Nakamura, and Y. Maeno, Phys. Rev. Mater. **8**, 074411 (2024).
[20] J. Zhang, A. S. McLeod, Q. Han, X. Chen, H. A. Bechtel, Z. Yao, S. N. Gilbert Corder, T. Ciavatti, T. H. Tao, M. Aronson, G. Carr, M. C. Martin, C. Sow, S. Yonezawa, F. Nakamura, I. Terasaki, D. N. Basov, A. J. Millis, Y. Maeno, and M. Liu, Phys. Rev. X **9**, 011032 (2019).
[21] I. Terasaki, I. Sano, K. Toda, S. Kawasaki, A. Nakano, H. Taniguchi, H. J. Cho, H. Ohta, and F. Nakamura, J. Phys. Soc. Jpn. **89**, 093707 (2020).
[22] K. Fürsich, J. Bertinshaw, P. Butler, M. Krautloher, M. Minola, and B. Keimer, Phys. Rev. B **100**, 081101(R) (2019).
[23] H. Vincent, D. Leroux, D. Bijaoui, R. Rimet, and C. Schlenker, J. Solid State Chem. **63**, 349 (1986).
[24] A. F. May, Y. Liu, S. Calder, D. S. Parker, T. Pandey, E. Cakmak, H. Cao, J. Yan, and M. A. McGuire, Phys. Rev. B **95**, 174440 (2017).
[25] A. F. May, H. Cao, and S. Calder, J. Magn. Magn. Mater. **511**, 166936 (2020).
[26] Y. Zhang, L.-F. Lin, A. Moreo, and E. Dagotto, Phys. Rev. B **107**, 054430 (2023).
[27] Y. Ni, H. Zhao, Y. Zhang, B. Hu, I. Kimchi, and G. Cao, Phys. Rev. B **103**, L161105 (2021).
[28] J. Seo, C. De, H. Ha, J. E. Lee, S. Park, J. Park, Y. Skourski, E. S. Choi, B. Kim, G. Y. Cho, H. W. Yeom, S.-W. Cheong, J. H. Kim, B.-J. Yang, K. Kim, and J. S. Kim, Nature (London) **599**, 576 (2021).
[29] Y. Liu, Z. Hu, M. Abeykoon, E. Stavitski, K. Attenkofer, E. D. Bauer, and C. Petrovic, Phys. Rev. B **103**, 245122 (2021).
[30] J. Wang, S. Wang, X. He, Y. Zhou, C. An, M. Zhang, Y. Zhou, Y. Han, X. Chen, J. Zhou, and Z. Yang, Phys. Rev. B **106**, 045106 (2022).
[31] R. A. Susilo, C. I. Kwon, Y. Lee, N. P. Salke, C. De, J. Seo, B. Kang, R. J. Hemley, P. Dalladay-Simpson, Z. Wang, D. Y. Kim, K. Kim, S.-W. Cheong, H. W. Yeom, K. H. Kim, and J. S. Kim, Nat. Commun. **15**, 3998 (2024).
[32] See Supplemental Material at http://link.aps.org/supplemental/10.1103/ry2d-bgyy, which includes Refs. [33–38], for additional information about the experimental methods and more detailed data.
[33] S. Middelhoek, J. Appl. Phys. **34**, 1054 (1963).
[34] K. Ramstfvöck, W. Hartung, and A. Hubert, Phys. Status Solidi (a) **155**, 505 (1996).
[35] S. Xu and D. J. Dunlop, Geophys. Res. Lett. **23**, 2819 (1996).
[36] L. Min, Y. Zhang, Z. Xie, S. V. G. Ayyagari, L. Miao, Y. Onishi, S. H. Lee, Y. Wang, N. Alem, L. Fu, and Z. Mao, Nat. Mater. **23**, 1671 (2024).
[37] Y. Tokura and N. Nagaosa, Nat. Commun. **9**, 3740 (2018).
[38] C. Ran, X. Mi, J. Shen, H. Wang, K. Yang, Y. Liu, G. Wang, G. Wang, Y. Shi, A. Wang, Y. Chai, X. Yang, M. He, X. Tong, and X. Zhou, Phys. Rev. B **108**, 125103 (2023).
[39] E. J. Ryder, Phys. Rev. **90**, 766 (1953).
[40] F. A. Chudnovskii, A. L. Pergament, P. Somasundaram, and J. M. Honig, Phys. Status Solidi (a) **172**, 131 (1999).
[41] A. Mohammadzadeh, S. Baraghani, S. Yin, F. Kargar, J. P. Bird, and A. A. Balandin, Appl. Phys. Lett. **118**, 093102 (2021).
[42] H. Ramamoorthy, R. Somphonsane, J. Radice, G. He, C.-P. Kwan, and J. P. Bird, Nano Lett. **16**, 399 (2016).
[43] T. Yasuda, M. Tonouchi, and S. Takano, Cesk. Cas. Fyz. **46**, 1265 (1996).
[44] Z. Peng, Y. Chen, and X. Feng, Int. J. Heat Mass Transfer **130**, 1170 (2019).
[45] Y. Zhang, Z. Li, K. Yang, L. Wei, X. Mi, A. Wang, X. Zhou, X. Yang, Y. Chai, and M. He, arXiv:2412.01518.
[46] Z. Liu, Z. Fang, H. Weng, and Q. Wu, arXiv:2503.19029.
[47] J. Fang, J. Hu, X. Chen, Y. Liu, Z. Yin, Z. Ying, Y. Wang, Z. Wang, Z. Li, S. Zhu, Y. Xu, S. T. Pantelides, and H.-J. Gao, 10.5281/zenodo.15468596, 2025.